Nuclear Inst. and Methods in Physics Research, A 959 (2020) 163479

Contents lists available at ScienceDirect

Nuclear Inst. and Methods in Physics Research, A

journal homepage: www.elsevier.com/locate/nima

Analysis and numerical design of Resistive AC-Coupled Silicon Detectors (RSD) for 4D particle tracking

M. Mandurrino [a,*], R. Arcidiacono [a,b], M. Boscardin [c,d], N. Cartiglia [a], G.-F. Dalla Betta [d,e], M. Ferrero [a,f], F. Ficorella [c,d], L. Pancheri [d,e], G. Paternoster [c,d], F. Siviero [a,f], V. Sola [a,f], A. Staiano [a], A. Vignati [a]

[a] INFN, Sezione di Torino, Via P. Giuria, 1, 10125 Torino, Italy
[b] Universitá del Piemonte Orientale, Largo Donegani, 2/3, 20100 Novara, Italy
[c] Fondazione Bruno Kessler, Via Sommarive, 18, 38123 Povo (TN), Italy
[d] TIFPA-INFN, Via Sommarive, 18, 38123, Povo (TN), Italy
[e] Universitá degli Studi di Trento, Via Sommarive, 9, 38123 Povo (TN), Italy
[f] Universitá degli Studi di Torino, Via P. Giuria, 1, 10125 Torino, Italy

ARTICLE INFO

Keywords:
TCAD modeling
Charge multiplication
Solid-state silicon detectors
Particle tracking detectors
Particle timing detectors
Fast detectors

ABSTRACT

In this paper we present the numerical simulation of silicon detectors with internal gain as the main tool for 4-dimensional (4D) particle trackers design and optimization. The Low-Gain Avalanche Diode (LGAD) technology and its present limitations are reviewed with the aim of introducing the Resistive AC-Coupled Silicon Detectors (RSD) paradigm as a case study of our investigation. Authors here present Spice-like and 2D/3D Technological Computer-Aided Design (TCAD) simulations to characterize sensors in terms of both their electrostatic behavior, capacitive (dynamic) coupling and radiation-hardness performances, showing the methodological approach used in order to extract the set of layout rules allowing the release of RSD1, the incoming production run at Fondazione Bruno Kessler (FBK) of next-generation silicon detectors for 4D tracking with intrinsic 100% fill-factor.

1. Introduction

Numerical simulation is an effective tools to design new detector structures and optimize existing devices. The technique described in this work is based on the well-known Technology Computer-Aided Design (TCAD) approach. By solving the Drift-Diffusion model for the structures under consideration through the commercial software Sentaurus Device by Synopsys, we are able to predict the general behavior of our devices as well as all the critical features characterizing their operation. Such procedure allowed to define the layout rules leading us to submit the lithographic masks of a first batch of Resistive AC-Coupled Silicon Detectors (RSD), produced by Fondazione Bruno Kessler (FBK) in Trento, Italy.

2. The role of RSD in 4D particle tracking

One of the most difficult challenges in silicon technology for 4D particle tracking is to combine the spatial and timing information while maintaining high levels of accuracy in both aspects. To this purpose, in the past years, the Italian National Institute for Nuclear Physics (INFN) in Torino developed the Ultra-Fast Silicon Detectors (UFSD), a project aiming at improving the measurement of particle arrival time through the LGAD paradigm [1,2]. Essentially, LGAD are *n*-in-*p* sensors ensuring fast and large signals thanks to a proper p^+-type *gain layer* implanted beneath the cathode. In reverse polarization regime, such layer is responsible for the multiplication of primary charges that are produced by traveling particles through the impact ionization of lattice atoms. By keeping the multiplication factor, or gain G, adequately low, it has been demonstrated that it is possible to have large output signal amplitude with, at the same time, a noise below the electronics readout noise [3].

For their timing performance, LGAD sensors have now been chosen for the upgrade of CMS and ATLAS experiments at CERN in view of High-Luminosity LHC (HL-LHC) [4]. In fact, with the expected luminosity in excess of about 10^{35} $cm^{-2}s^{-1}$, between 10%–20% of vertices identified by the inner tracking detector will be composed by the overlap of two subsequent pp collisions that happen so close to each other in space to be mistakenly interpreted as a single interaction. The only way to correctly disentangle such vertices is to measure the time of each track: as the interactions of each bunch crossing occur randomly in a time spread of the order of 150 ps, measuring the time of each track

* Corresponding author.
E-mail address: marco.mandurrino@to.infn.it (M. Mandurrino).

https://doi.org/10.1016/j.nima.2020.163479
Received 29 April 2019; Received in revised form 13 January 2020; Accepted 19 January 2020
Available online 22 January 2020
0168-9002/

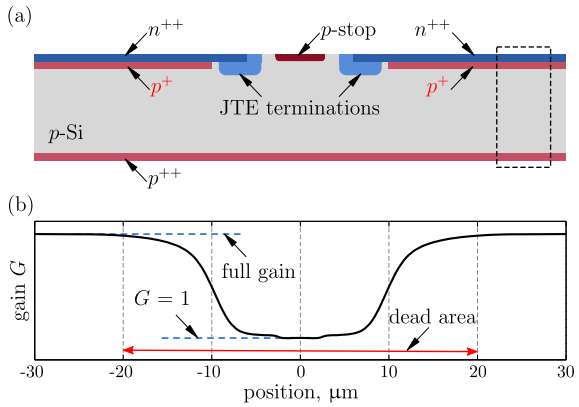

Fig. 1. (a) Cross section of the segmentation structures between two adjacent LGAD active areas and (b) gain G as a function of the particle hit position calculated through numerical simulations. In the dashed rectangle: simple-2D slice including only the essential LGAD implants to be used in simplified simulations.

with an accuracy of about 30–35 ps can remarkably reduce the overlap, allowing current reconstruction algorithms to distinguish almost always the two collisions.

To obtain also a good spatial granularity with fast signals, one of the most used solutions is to implement LGAD sensors with patterned sensitive areas, where each pixel unit is identified by its gain implant. An important implication of such segmentation scheme is the need to avoid early breakdown at pixel edges and short-circuit between nearby pixels. This is achieved through the implantation of proper termination structures between sensitive areas which are, respectively, the JTE and *p*-stop implants depicted in Fig. 1(a). This set of features, which compose the inter-pixel segmentation, determines a dead area (or no-gain area) for particle detection, having charge multiplication only when the particle passes through a gain area and not in the inter-pixel regions. To this purpose, it is useful to introduce the concept of *fill-factor*, which is defined as the ratio between the gain area and the total area. Panel (a) of Fig. 1 shows the segmentation structures between two adjacent pixels of an LGAD sensor along with, in panel (b), the gain behavior as a function of the longitudinal position where the charged particle hits the sensor. Due to hermetic coverage required by high-luminosity experiments – e.g., fill-factor must be > 95% in the CMS MIP Timing Layer (see, for instance, Refs. [4,5]) – the need of new technologies arises since, even though the smallest possible layout rules are implemented, the dead area cannot be made smaller than ∼40 μm. This dimension results from the combination of two effects: (*i*) the physical distance between gain implants, also inclusive of their lateral spreading distributions, and (*ii*) the effective gain turn-on, determined by the shape of field lines in silicon.

To get rid of any gain loss due to segmentation structures, we designed Resistive AC-Coupled Silicon Detectors (RSD), which essentially are LGAD optimized for both spatial and timing detection (4D-tracking) with high segmentation level [6]. They are currently being developed in Torino under a contract framework between INFN and FBK. Benefiting from the experience gained in the LGAD framework in terms of radiation hardness and time resolution, their process flow is almost as simple as that of the LGAD. This translates into low-budget production costs and large areas implementation. The RSD operation principle is based on the resistive AC-coupled readout, as shown in panel (a) of Fig. 2, where the detector bulk is modeled by a grid of capacitors C_{det} connected to a resistive n^+ layer of a given sheet resistance R_{sheet} (∼kΩ). The readout takes place via AC-coupling capacitors C_{AC}, designed to induce a signal on the metal pads. In this layout the resistive electrode is required to be such that the multiplied charges are kept frozen for a characteristic time sufficient to guarantee the complete signal induction before being discharged, but also short enough to minimize pile-up effects. Then the discharge occurs through proper DC contacts (not represented in Fig. 2) that are usually located at the device periphery, on the front side.

Having such readout scheme, with signals that are locally induced on the pad where charges have been generated, RSD do not require the segmentation layout proper of standard technology. For this reason they can be realized with both continuous gain layer and *n*-electrode implants, allowing spatial reconstruction of tracks with a fill-factor intrinsically equal to 100%. A drawback of the RSD technology might be represented by the charge sharing between adjacent pads, that can be kept under control by an accurate engineering of the doping profile working as cathode layer and, in turn, of its effective sheet resistance. Panels (b) and (c) of Fig. 2 show, respectively, the cut of an RSD device (notice the continuity of the p^+ gain layer) and its simplified circuital model for a single node of the electrical grid. As one may note, the resistive stage is implemented through an optimized version of the usual *n* layer, while the AC-coupling is realized by placing a capacitive dielectric spacer between silicon and readout electrodes. In this new paradigm, both the cathode and the gain layer remain homogeneous and constant along the sensor area, creating an almost uniform electric field. It is a key element of the design that, even though the volume of the whole sensor might be rather large, each AC readout pad, due to the resistive sheet, is sensitive only to a small region of the detector (or, in other words, to the local value of C_{det}), and it will be almost uncorrelated to the total leakage.

3. Modeling methods and simulation

In order to calculate the signal generated by the RSD under irradiation, 1D preliminary TCAD simulations using the drift-diffusion (DD) framework have been used (see [7,8] as previous references for numerical simulation of charge multiplication in silicon particle detectors). Then, the output waveforms are implemented into Spice to simulate the electrical behavior of a full sensor module and extract the most important design parameters, i.e. the electrode resistivity, the oxide thickness with its capacitance and the pad size and pitch. After this calibration, 2D and 3D simulations have been performed with a TCAD tool in order to characterize the RSD devices in terms of charge multiplication, static/dynamic electrical properties (such as $C(V)$, $I(V)$, charge sharing or signal capacitive coupling), radiation resistance and, consequently, to define all the layout rules for the first production run of sensors.

3.1. The drift-diffusion framework

For the purposes explained in the introduction, we have chosen to use a commercial tool [9] based on the drift-diffusion (DD) model, where the Poisson equation of semiconductors

$$\nabla^2_{\mathbf{r}}\,\varphi(\mathbf{r},t) = -\frac{\rho(\mathbf{r},t)}{\epsilon}\,, \tag{1}$$

describing the coupling between the electric field $\mathcal{E} = -\nabla_{\mathbf{r}}\,\varphi$ and the total charge density $\rho = q\,(p - n + C)$, is self-consistently solved with the continuity equations for electrons and holes

$$\begin{aligned}\frac{\partial n(\mathbf{r},t)}{\partial t} &= +\frac{1}{q}\nabla_{\mathbf{r}}\,J_n(\mathbf{r},t) - U_n(\mathbf{r},t)\\ \frac{\partial p(\mathbf{r},t)}{\partial t} &= -\frac{1}{q}\nabla_{\mathbf{r}}\,J_p(\mathbf{r},t) - U_p(\mathbf{r},t)\end{aligned} \tag{2}$$

where φ is the electrostatic potential, ϵ the isotropic dielectric constant, q is the elementary charge, p, n and C are, respectively, the density of holes, electrons and fixed charges (like defects and traps), $J_{n,p}$ is the electron/hole current density and $U_{n,p}$ the net generation/recombination (GR) rate of charge carriers, i.e. the number of electron/hole pairs generated or recombined per cm^3 in the unit time. Within the DD framework

$$U(\mathbf{r},t) = G(\mathbf{r},t) - R(\mathbf{r},t)\,, \tag{3}$$

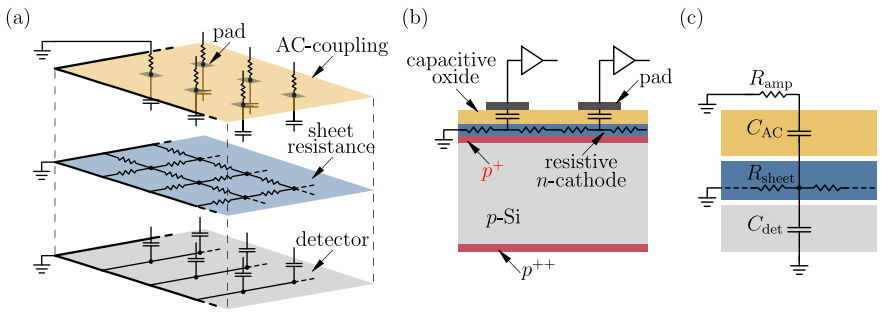

Fig. 2. Basic operational principles of the resistive AC-coupled readout: (a) Electronic equivalent circuit. (b) Cross-sectional sketch of a silicon n-in-p RSD where the n-type cathode, freezing the charges, and a cap dielectric, to allow the signal transfer to the pads by capacitive induction, are represented. (c) Circuital model in correspondence of a single node of the resistive sheet, i.e. for a readout pad.

where G and R terms respectively represent the generation and recombination rates, and all current densities are computed as a sum of a drift contribution, driven by the electric field, and a diffusion component, determined by the gradient of charge concentration so that, for electrons,

$$J_n(\mathbf{r},t) = J_n^{\text{diff}}(\mathbf{r},t) + J_n^{\text{drift}}(\mathbf{r},t) = q\left[D_n \nabla_{\mathbf{r}}\, n(\mathbf{r},t) - \mu_n \left(\nabla_{\mathbf{r}}\, \varphi(\mathbf{r},t)\right) n(\mathbf{r},t)\right] \tag{4}$$

and similarly for holes, where

$$D_{n,p}(\mathbf{r},t) = \mu_{n,p}(\mathbf{r},t)\frac{k_B T}{q} \tag{5}$$

are the Einstein diffusion coefficients for electrons and holes, $\mu_{n,p}$ their mobilities, written as

$$\mu_{n,p}(\mathbf{r},t) = \frac{v_{n,p}^{\text{drift}}}{\mathcal{E}(\mathbf{r},t)} = -\frac{v_{n,p}^{\text{drift}}}{\nabla_{\mathbf{r}}\, \varphi(\mathbf{r},t)}\,, \tag{6}$$

and $v_{n,p}^{\text{drift}}$ are the electron/hole drift velocities due to the local internal field $\mathcal{E}$.

To solve the set of partial differential equations (PDE) composing the DD model written in Eqs. (1)–(2), we have to adopt a scheme for sampling all the physical quantities to be computed inside the detector of our interest and linearize the system. To this purpose the device geometry is discretized with the Scharfetter–Gummel triangulation procedure and, by applying proper boundary conditions (BC), the DD system is linearized through a finite boxes (FB) approach and then is solved with the Newton iterative method at each node of the discretization grid. The GR mechanisms accounted for as proper net rates U are the Shockley–Read–Hall (SRH), band-to-band tunneling (BTBT) and avalanche impact ionization. In particular, charge multiplication has been implemented by means of three commonly used models: Massey, van Overstraeten–de Man and Okuto-Crowell model (see Refs. [10–12]). They are all describing the avalanche charge multiplication in silicon as

$$U_{\text{aval}} = \alpha_n n v_n + \alpha_p p v_p\,, \tag{7}$$

where U_{aval} is the net GR rate for the avalanche ionization, $v_{n,p}$ are the total carrier velocities and $\alpha_{n,p}$ represent the electron/hole ionization coefficients (in cm^{-1}), whose expression, following the well-known Chynoweth law [13], varies according to the specific formalism we are taking into account. In particular, for the Massey model – that we implemented as an external C++ routine via the Sentaurus PMI (Physical Model Interface) tool, being not included among the built-in functions – we have

$$\alpha_{n,p}^{\text{Mas}}(\mathcal{E}) = A_{n,p}^{\text{Mas}} \exp\left(-\frac{B_{n,p}^{\text{Mas}}(T)}{\mathcal{E}}\right), \tag{8}$$

while, in the van Overstraeten–de Man approach

$$\alpha_{n,p}^{\text{vOv}}(\mathcal{E}) = \gamma\, A_{n,p}^{\text{vOv}} \exp\left(-\gamma \frac{B_{n,p}^{\text{vOv}}}{\mathcal{E}}\right) \tag{9}$$

and, finally, the Okuto–Crowell formalism reads

$$\alpha_{n,p}^{\text{Oku}}(\mathcal{E}) = A_{n,p}^{\text{Oku}}\left(1 + (T-300)\, C_{n,p}^{\text{Oku}}\right)\mathcal{E} \times \exp\left[-\left(\frac{B_{n,p}^{\text{Oku}}\left(1 + (T-300)\, D_{n,p}^{\text{Oku}}\right)}{\mathcal{E}}\right)^2\right], \tag{10}$$

where the pre-factor A (in cm^{-1}), the critical field B (V/cm), the coefficient γ, C and D (both in K^{-1}) are different in the three models (see the Appendix or Ref. [7]).

By imposing proper initial conditions (IC) at the device electrodes and an initial guess for the electrostatic potential φ, the TCAD solver can self-consistently evaluate all the nodal unknowns, such as the electron/hole carrier and current densities (n, p and $J_{n,p}$), as well as the device-level macroscopic output quantities (total current flowing through the detector, capacitance or induced signals).

3.2. Radiation damage modeling

Being the RSD technology conceived to operate also in radiation-intense frameworks, its TCAD-based design and optimization has to necessarily include the role of lattice damaging mechanisms. The evidence of trap states production in silicon under irradiation has been extensively reported in literature since 50s of the last century (see, for instance, Ref. [14]), and it can be simply managed from the numerical viewpoint by introducing proper *ad-hoc* empirical laws for each family of defects where the overall trap density is modeled through a certain function of the radiation fluence ϕ (in cm^{-2}).

But the phenomena which we are more interested in are some crystal-level modifications occurring to dopant atoms in correspondence of the multiplication implant and, in particular, the mechanisms known in the literature as *acceptor deactivation* (sometimes also going under the less proper name of acceptor removal). Indeed, more recent observations [15] reported that the active (substitutionals) acceptor elements are removed from their lattice sites due to a two-step process: (*i*) the radiation produces interstitial Si atoms that subsequently (*ii*) capture and deactivate the doping elements via kick-out reactions (Watkins mechanism [16]) producing ion-acceptor complexes (interstitials) [17].

The strategy we used to introduce both the defect production and deactivation mechanisms in our simulations consists in an off-line recomputation of the gain layer and acceptor bulk profiles according to the model [2]

$$N_{\text{A}}(\phi, x) = g_{\text{eff}}\,\phi + N_{\text{A}}(0,x)\, e^{-\phi\, c\left(N_{\text{A}}(0,x)\right)}\,. \tag{11}$$

Here the resulting acceptor concentration, function of both the fluence ϕ and the initial (nominal) acceptor density $N_{\text{A}}(0,x)$, is the linear combination of a term accounting for the effective generation of traps, $g_{\text{eff}}\,\phi$, and an exponential contribution coming from the acceptor deactivation occurring within the p^+-type gain layer. In the case of LGAD

technology, it has been empirically proven that $g_{\text{eff}} \simeq 0.02$ cm^{-1} provides a good description of the first mechanism [18,19].

In Eq. (11), the acceptor deactivation coefficient $c\left(N_{\text{A}}(0,x)\right)$ (in cm^2) is the inverse of the fluence needed to reduce the initial doping density $N_{\text{A}}(0,x)$ by a factor 1/e, and has been empirically modeled by (see details in Ref. [19])

$$c\left(N_{\text{A}}(0,x)\right) = k_{\text{c}}\,\frac{N_{\text{Si}}\cdot N_{\text{int}}\cdot\sigma_{\text{Si}}}{0.63\cdot N_{\text{A}}(0,x)}\,\frac{1}{1+\left(\frac{N_{\text{A,crit}}}{N_{\text{A}}(0,x)}\right)^{\frac{2}{3}}}\,, \tag{12}$$

where k_{c} is the probability of capturing a doping element, σ_{Si} (in cm^{-2}) the Silicon cross-section of the scattering process with the ionizing particle, N_{Si} ($5\cdot10^{22}$ cm^{-3}) and N_{int} (in cm^{-3}) are, respectively, the Silicon atomic density in the lattice and the concentration of interstitials created by radiation and, finally, where $N_{\text{A,crit}}$ (in cm^{-3}) is an empirical fitting parameter indicating the critical acceptor concentration at which the interstitial Silicon atoms have a probability of 0.5 to capture and deactivate an acceptor state.

From such model the fact that the acceptor density profile has to be corrected locally (in space x) comes quite straightforwardly. Furthermore, it has to be noticed that parameters N_{int}, σ_{Si} and $N_{\text{A,crit}}$ may assume different values depending on whether we irradiate silicon detectors samples with protons or neutrons, while the value of k_{c} is mainly subjected to the chemical nature of acceptor dopants used in the gain layer (e.g., Boron or Gallium) and for the bulk doping.

3.3. Calibration of the minimum ionizing particle (MIP) energy release

In reverse bias and full-depletion conditions, and with electrons and holes at their saturation velocity, primary charges generated by an ionizing particle drift towards their respective electrodes: electrons to the *n*-cathode and holes to the *p*-anode. When such electrons drift across the gain layer, they experience the high electric field responsible for the multiplication mechanism and participate to the phenomenon of avalanche impact ionization. For each primary electron a certain number of secondary (multiplied) electron/hole pairs are generated through the further ionization of silicon atoms. This number is a function of the electron velocity which, in turn, directly depends on the electric field and, finally, on the applied reverse bias. This is the reason why, near a threshold field (~300 kV/cm), there is the onset of an exponential-like trend of the detector gain G as a function the increasing bias.

In order to study the charge multiplication after the passage of a charged particle, we activated in Sentaurus the Heavy Ion function, which emulates an ion traveling through the detector. This function allows the user to control the amount of ionization energy released by the ion, that we want to set as the Minimum Ionizing Particle (MIP) energy. Typically, a MIP provides an energy large enough to produce approximately 75 electron/hole pairs every micron of silicon crossed. To correctly calibrate such number, we proceeded to test our modeling framework by comparing simulated and measured collected charges in silicon detectors coming from different vendors. In a first phase, such calibration has been performed with *p-i-n* diodes, i.e. detectors without the internal multiplication layer, where the gain is only due to avalanche processes in the bulk under very-high electric field conditions.

By simulating the transient through which an heavy ion transfers its energy to the silicon lattice, the DD model is able to predict the number of electron/hole pairs generated at a given external voltage and then multiplied in the gain layer. Indeed, once one of the discussed avalanche models has been selected, its related net GR rate U_{aval} written in Eq. (7) can be evaluated. Then, the avalanche impact ionization contribution to the total current density is computed at run-time in all the mesh nodes by self-consistently solving the electron/hole continuity equations. The generated and multiplied charges are collected by electrodes and give origin to a current pulse which is the result of: (*i*) an induced current component $i^{\text{ind}}(t)$ due to the charge carriers flowing underneath the electrode itself, as stated by the Shockley–Ramo theorem [20,21]

$$i^{\text{ind}}_{n,p}(t) = q\,\mathcal{E}_w\,v^{\text{drift}}_{n,p}\,, \tag{13}$$

where $\mathcal{E}_w$ is the so-called *weighting field*, and (*ii*) the current contribution $i^{\text{col}}(t)$ due to the carriers physically collected by the same electrode. Integrating in time the total current pulse $i_{n,p}(t) = i^{\text{ind}}_{n,p}(t) + i^{\text{col}}_{n,p}(t)$ we can compute the amount of multiplied charge and, then, the detector gain at a given bias. Notice that, in RSD, physical collection of charge at readout electrodes does not take place anymore, since the signals are exclusively due to a capacitive coupling induced by the dielectric separation layer (see Fig. 2). The discharge will only occur through proper DC contacts representing the grounded path for electrons.

Fig. 3 shows the comparison between simulated and measured collected charge as a function of the reverse applied voltage for 1 MIP in two irradiated *p-i-n* diodes coming from different foundries: Centro Nacional de Microelectrónica (CNM), in Barcelona, and Hamamatsu Photonics K.K. (HPK), Japan [22]. In the following we will refer quite indifferently to collected charge as to $G(V)$ characteristics, since the gain G of an LGAD is obtained dividing the charge multiplied in the detector with internal gain by the charge collected in the corresponding device without the multiplication layer. In *p-i-n* diodes, instead, the $G(V)$ curve can be simply constructed by dividing the number of charges read at the electrode at a given bias by the charges collected in low-injection regime (where there is no avalanche, and $G = 1$).

The good agreement between simulations and measurements shown in Fig. 3 has been obtained by setting an ionizing energy transfer equal to 56 and 70 pairs per micron, respectively, and by using all the three avalanche formalisms to model the ionization coefficients $\alpha_{n,p}$. Moreover, in order to take into account the effects of radiation in silicon, the trap generation law $N_{\text{A}}(\phi) = g_{\text{eff}}\,\phi$ has been implemented. The difference we observe about the number of generated pairs in the samples under investigation from the typical value of 75 electron/hole pairs may be due to the uncertainty on the true active thickness, or can be the effect of local discrepancies or fluctuations around the nominal value of 50 μm. Nevertheless, such difference simply reflects the necessity to calibrate our numerical setup, and gives an indication of the modeling limitations. Moreover, as one may appreciate, Massey and van Overstraeten–de Man models reproduce the measured charge with a better accuracy.

As already said, being without any gain implant, *p-i-n* diodes have a multiplication onset occurring at relatively high applied bias. This occurs because the only contribution to the avalanche mechanism comes from the bulk, thus the electric field has to be raised along the whole device depth, which means a high potential difference before exceeding the threshold field. So our procedure is useful to set the $G(V)$ baseline in low-bias conditions (i.e. the number of deposited primary charges) when the multiplication factor is unitary rather than for describing its exponential growth. At any rate, Fig. 3 demonstrates that – at least in this temperature range and for the devices of our analysis – the Massey model reproduces quite well the measured $G(V)$ trend also in the high-injection regime.

In order to have an even more robust numerical setup, the same calibration has been performed by simulating the diode under the stimulus of a laser beam. This procedure allows us to compare the calculated $G(V)$ curves also with experimental data where the charge ionization is provided through the IR light and not by ion irradiation as, for instance, in Transient Current Technique (TCT) measurements [24]. We found that an optimum agreement can be found between $G(V)$ curves simulated with heavy ions producing 56 pairs per micron and with an IR laser ($\lambda = 1060$ nm) releasing the energy density of 310 W/cm^2. The most important difference between using the IR laser or the heavy ion is that, if necessary, in the first case the software allows to use an illumination window with a finite width. This allows to implement a certain intensity profile, very useful when comparing simulations and TCT measurements, as mentioned before. Nevertheless, once the MIP has been calibrated in the experimental setup, there is no difference between signals generated with a laser or with particles.

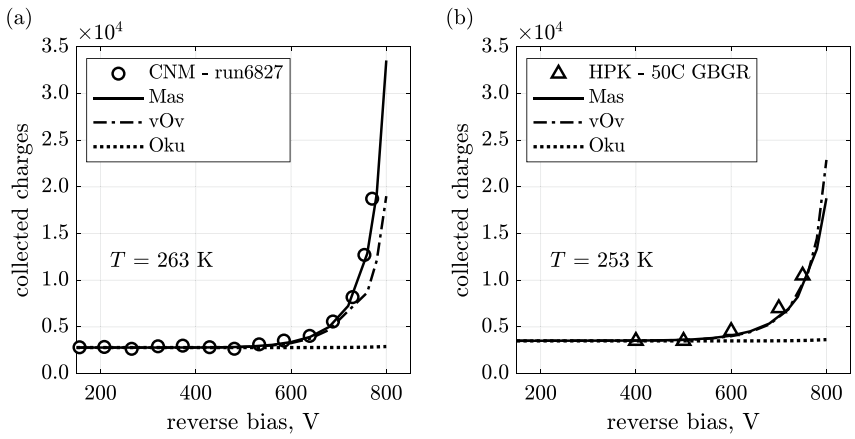

Fig. 3. Measured (symbols) and simulated (lines) collected charge (or gain) for 1 MIP in 50 μm-thick devices: (a) *p-i-n* diode irradiated with neutrons at $\phi = 3 \cdot 10^{15}$ n_{eq}/cm^2 and (b) pions at $\phi = 1.5 \cdot 10^{15}$ n_{eq}/cm^2, respectively. Experimental data presented in Refs. [7,22,23].

3.4. Simple-2D TCAD simulations of avalanche diodes

Once we calibrated our numerical setup on the simple *p-i-n* diodes, we can solve the DD diffusion model for an LGAD in order to find the avalanche model that better reproduces the gain in the devices under consideration. By implementing a simplified quasi-2D geometry which includes only the most important implants without any transversal dependence, as indicated by the dashed box in Fig. 1(a), we can predict some important detector characteristics, such as $I(V;T)$ and $G(V;T)$, before or after irradiation, and below the Geiger operation mode (i.e. in the moderate-gain regime). As an example, Fig. 4 shows the measured and calculated gain for an unirradiated 50 μm-thick LGAD sample by HPK as a function of the applied bias as well as the temperature. The three avalanche models have been applied after emulating a laser beam with energy density deposited of 310 W/cm^2, while the gain has been computed by simulating both the device with the multiplication layer and its related *p-i-n* diode and then by dividing, for each bias point, the number of charges collected in the LGAD by the charges produced in the version without gain of such device.

Again, as in the previous simulations, Massey model provides the best-fitting agreement with the available experimental data, at least for the bias and temperature range at our disposal.

To test the effectiveness of the radiation damage model presented in the previous sections we proceeded by comparing our simulations with gain measurements coming from irradiated detectors. Panel (a) of Fig. 5 shows both simulated and experimental collected charges in an LGAD sensor by FBK at different fluences, from the non-irradiation condition to $\phi = 5 \cdot 10^{14}$ n_{eq}/cm^2. Even if also temperature is changing among samples, the van Overstraeten–de Man model is able to predict quite well all the curves of charge versus applied bias. All the calculated charges are simulated through the laser beam approach, with a released energy density of 310 W/cm^2.

Moreover, in panel (b), one can find the trend of the bias required to collect 20k electrons as a function of the fluence for different LGAD sensors produced by CNM and HPK. Here simulations have been obtained by using the Heavy Ion function, generating 56 pairs per micron.

The plots included in Fig. 5 reflect the robustness of the empirical radiation damage parametrization written in Eq. (11) in describing the charge multiplication mechanism for irradiated LGAD-based particle detectors. Nevertheless, another important aspect is the precision level in catching by numerical simulation the onset bias of the multiplication process as a function of the gain dopant dose and species, which represents an essential feature in developing new detectors. Before implementing the usual static simulations in order to study the collected charge at different bias voltages, we tested the gain profiles by comparing simulated and measured $C(V)$ characteristics (both performed with 1 kHz AC signals) for different samples coming from the run UFSD2 [27], a second production of 50 μm-thick LGAD detectors designed at Trento University and produced by FBK in 2017. In panel (a) of Fig. 6, the measured capacitance characteristics have been used to extract the acceptor profiles (regarding this procedure see, for instance, Ref. [19]) that have been included in the solver as input data of our simulated $C(V)$. This important cross-check strategy represents a robust proof about the reliability of our numerical setup, being the agreement between experimental data and simulations highly satisfactory. In particular, both the kink at low bias and the subsequent foot before the baseline (corresponding respectively to the depletion of gain layer and active volume) are perfectly modeled by TCAD.

Having verified that the solving architecture works properly, we used the same setup to simulate the $G(V)$ characteristics of four unirradiated UFSD2 samples differing for the gain layer dopants: Gallium, Gallium with Carbon co-implantation, Boron and Boron with Carbon co-implantation. Both the Gallium and Carbon implants represent two R&D solutions to mitigate the radiation damage in Silicon and, in particular, the effects of acceptor deactivation mechanism [19]. Panel (b) of Fig. 6 shows the satisfactory results of comparing measured and simulated gain curves for the samples described above, where the van Overstraeten–de Man model with the Heavy Ion energy release has been implemented. Such simulations are obtained with the usual strategy of implementing both the LGAD and the *p-i-n*, and then performing the ratio between their respective collected charges.

The last basic feature to be analyzed is the modeling sensitivity to the gain layer doping dose and, in particular, the shift of the multiplication onset towards low bias values with the increasing acceptor density. To this purpose, several 300 μm- and 50 μm-thick LGAD structures respectively coming from FBK and HPK, and (slightly) varying in their multiplication layer profiles, have been simulated. In the case of FBK detectors, the dose increases for higher wafer numbers W while, in HPK sensors, the higher the letter progressively labeling the device the greater the dopant dose. Again, both LGAD and *p-i-n* devices have been implemented.

As reported in Fig. 7, our numerical setup is perfectly sensitive to dose variations in the gain layer. Moreover, both Massey and van-Overstraeten–de Man formalisms well reproduce the experimental curves.

3.5. Electric field simulations

In the standard LGAD technology for particle tracking, one figure of merit to be carefully optimized with the simulator before designing the final detector layout is the electromagnetic insulation between sensitive areas, i.e. at the level of inter-pixel termination structures, as well as in correspondence of the external guard region, designed to allow a

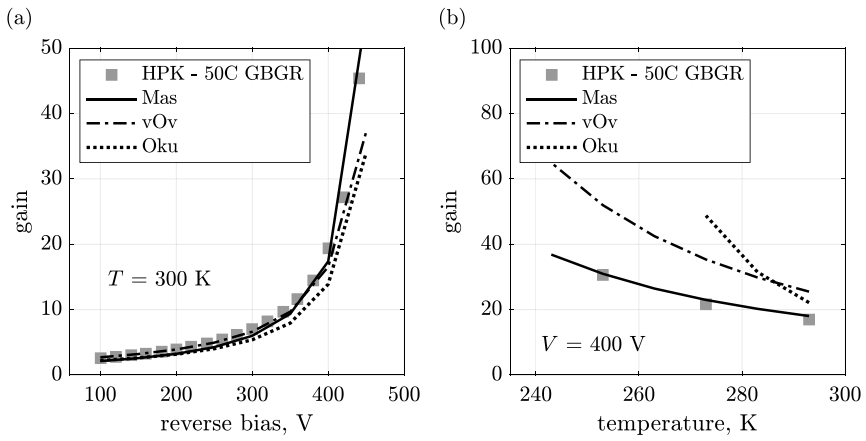

Fig. 4. Comparison between measured (symbols) and simulated (lines) gain in unirradiated 50 μm-thick LGAD sensors by HPK as a function of (a) applied bias and (b) temperature. Experimental data taken at HPK and presented in Refs. [7,25].

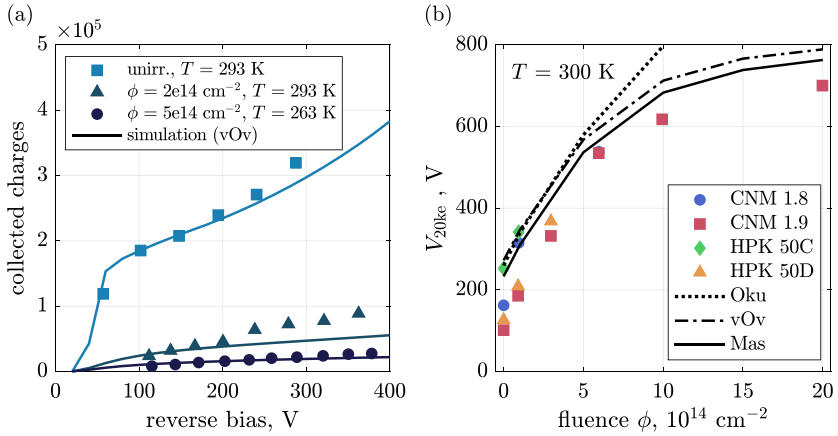

Fig. 5. Measurements (symbols) and simulations (lines) of (a) charges versus bias in an irradiated 300 μm LGAD sensor by FBK and (b) bias to collect 20k electrons as a function of fluence in 50 μm-thick LGAD sensors by HPK and CNM. Experimental data presented in Refs. [7,23,26].

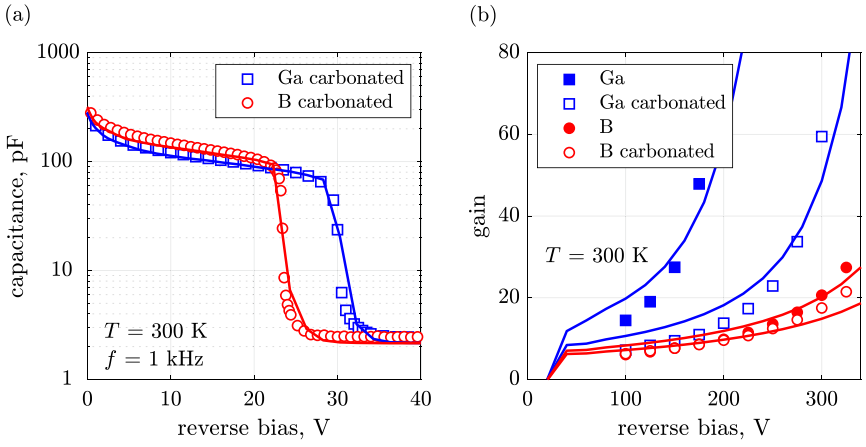

Fig. 6. Unirradiated detectors. Panel (a): measured (symbols) and simulated (lines) $C(V)$ characteristics in Gallium and Boron carbonated 50 μm-thick LGAD from UFSD2 production run by INFN and FBK. Simulations are performed by generating electron/hole pairs with the heavy ion approach and by injecting a sinusoidal bias at 1 kHz. Panel (b): comparison between experimental and numerical $G(V)$ characteristics for several UFSD2 devices.

correct scaling of bias voltage when the lithographic approach becomes more aggressive. Moreover, as we have already seen in the previous sections, such traditional silicon detectors are affected by the signal (or gain) loss at the pixel periphery, so that a critical trade-off between layout and efficiency has to be found.

We extensively explored such topics with numerical simulations when designing at INFN Torino, and in collaboration with FBK, the last three runs of UFSD devices. And now we are facing with the new challenges of optimizing our detectors in view of the upcoming productions for the HL-LHC timing layers and within the RSD project. To this purpose, we have to abandon the simplified quasi-2D modeling scheme introduced in the previous section in favor of a more realistic simulation framework, where all the oxide and metal layers have to

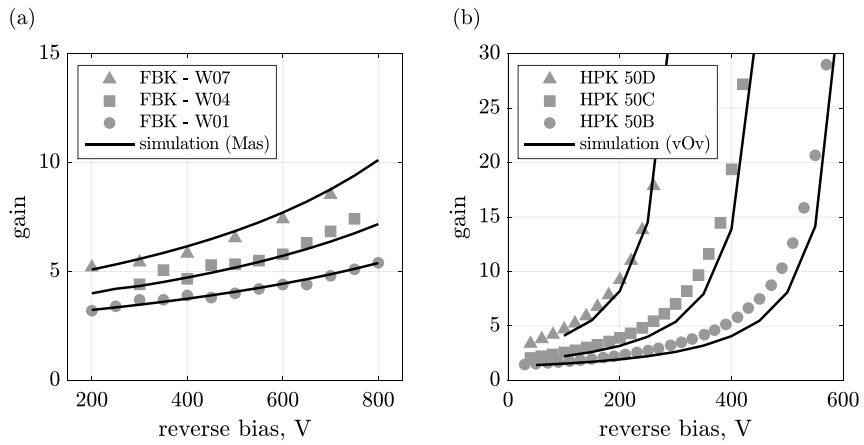

Fig. 7. Room temperature comparison between measured (symbols) and simulated (lines) $G(V)$ characteristics in (a) 300 μm-thick LGAD detectors from UFSD1 production run by INFN and FBK (with the wafer number W increasing with the gain implant dose) and (b) 50 μm-thick LGAD devices by HPK (where, again, the last letter increases with the increasing boron dose).

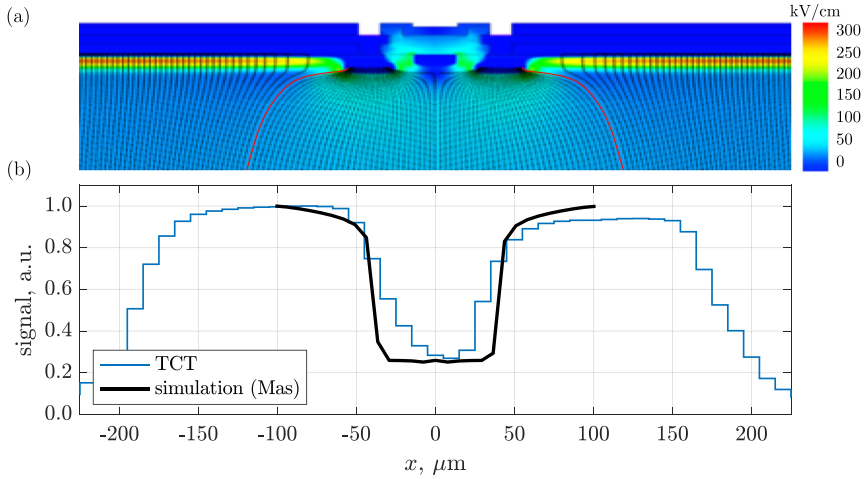

Fig. 8. Panel (a): simulated electric field (intensity color map) and drift lines in the inter-pixel region of an LGAD device. Panel (b): comparison between measured (histogram) and simulated (curve) signal amplitude versus position for an IR laser scan carried out along a 200 μm-pitch LGAD strip-detector. Note: pictures (a) and (b) are not to the same scale. (For interpretation of the references to color in this figure legend, the reader is referred to the web version of this article.)

be implemented and in which also all the implants with their lateral spreading functions are necessarily accounted for.

An example of this study can be found in panel (a) of Fig. 8, which shows the field intensity color map, along with the drift lines, simulated in an inter-pixel region between two LGAD sensitive areas under reverse bias conditions. Red curves inside the detector, representing the outermost drift lines closing on JTE terminations, are one of the most crucial parameters in shaping the signal as a function of the horizontal position x. The drift lines in the middle determine the width of the no-gain area.

Panel (b) of Fig. 8 reports the signal amplitude generated by a laser ($\lambda = 1060$ nm), shined from the top to emulate the charged particles traversing the device vertically, scanning the inter-pixel region of a reversely biased (230 V) 200 μm-pitch LGAD strip-detector from the UFSD2 run by FBK. Measurements have determined a no-gain FWHM of 75 μm while from simulation (with Massey model) we found 78 μm. Notice also that the calculated curve has a sharper profile with respect to what has been experimentally obtained. This could probably be the effect of difference in two setups. Indeed, the laser has a finite spot size (∼15 μm), and this contributes to obtain a signal transition between gain and no-gain zone which is due to the convolution of an electric field, varying with depth, evaluated on a finite volume of silicon. On the other hand, simulations are based on a point-like laser beam, which results in a signal trend more conformal to the internal structure of drift lines, revealing further details about the field. This makes the latter approach more suitable for a comparison with data coming from test beams with particles rather than with the laser. Anyway, the agreement is such that we can confidently use point-like simulations to have a rough estimation about the fill-factor in traditional silicon detectors for particle tracking. Otherwise, a finite spot size laser beam can be used also in TCAD simulations.

4. Simulation of RSD

4.1. Edge effects in the p^+-type gain layer

In RSD, despite the lack of termination implants, there are some electromagnetic properties that can potentially affect the normal device operation. As an example, an important aspect to be taken into account is the electric field trend along the resistive sheet in correspondence of the gain layer starting point. Panel (a) of Fig. 9 reports the typical cross section of an RSD at its peripheral zone, where the DC-contacts collecting all the multiplied charges are usually located. Having a p-gain implant which starts in between the DC-electrode and the coupling region determines (at a given bias) a longitudinal variation of the multiplication field. The gradient of such field has to be carefully investigated through numerical simulations in order to avoid any gain

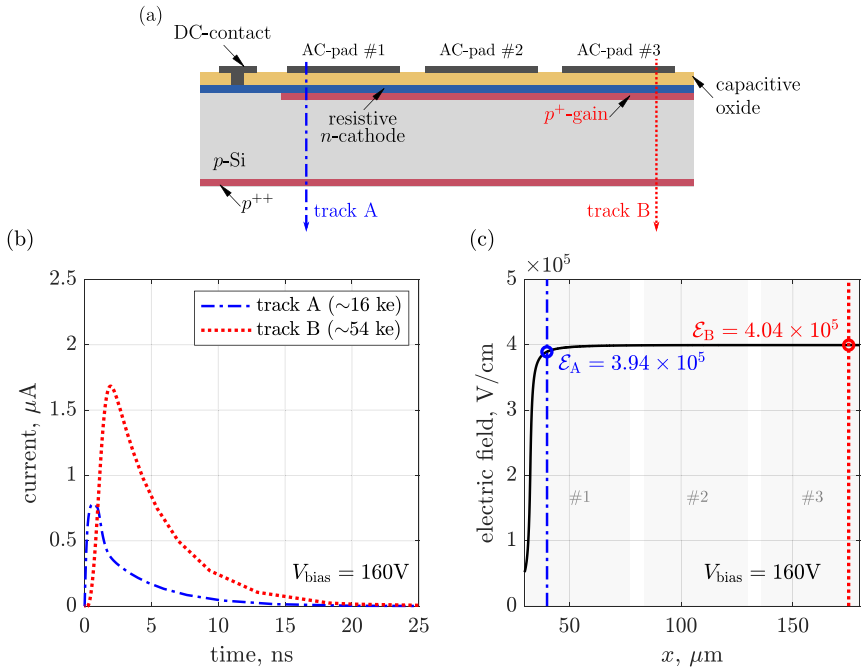

Fig. 9. Panel (a): schematic cross section of the simulated RSD (not to scale), where two heavy ion MIP tracks have also been represented. Panel (b): current signals read at the DC-contact for the two tracks A and B (legend reports the corresponding number of collected charges). Panel (c): electric field along the resistive cathode; vertical lines represent the position of the tracks while labels indicate the field at that coordinates.

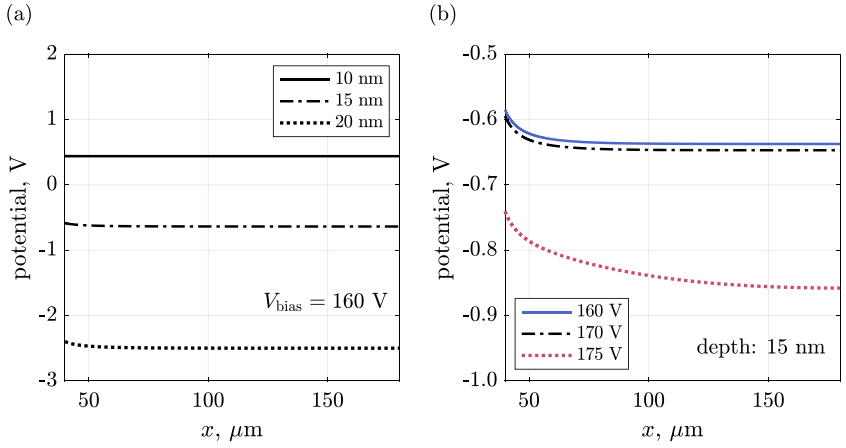

Fig. 10. Horizontal trend of the electrostatic potential simulated in the RSD device represented in the cross section of Fig. 9 as a function of (a) depth with respect to the Silicon/oxide interface, at fixed bias $V_{bias} = 160$ V, and (b) at different applied bias, at a fixed depth of 15 nm.

loss that may compromise the detector overall efficiency and, in turn, its timing performance.

In order to find a safety distance from the gain implant boundary to the AC-coupled readout pads, the 2D domain reported in panel (a) of Fig. 9 has been implemented in TCAD, where the thickness is 55 μm. Then, we raised the external bias voltage to −160 V and we simulated two different tracks produced by heavy ions passing through the RSD at 40 μm and 175 μm from the left edge of the gain implant, that is, respectively, in correspondence of the AC pads #1 and #3 (as drawn in panel (a) with the dot-dashed and dotted arrows). From the electric field profile obtained along an horizontal cut passing through the resistive sheet – see panel (c) – we found that the field rise is confined in a region as wide as ∼30 μm, if assuming a tolerance of 5%. This is true, at least, for the specific implants used in the LGAD technology and, in particular, for the RSD process. Notice also that, as the current waveforms read by the DC-contact are showing in panel (b), the signal generated by the track A results to be heavily degraded with respect to the other one coming from track B, both in terms of peak amplitude and total collected charge (reported in the plot legend). This is mainly due to the lower gain experienced by the ion passing through the unsafe region (otherwise the collected charges would be the same) and, in part, to the propagation of signals from points at different distances from the DC-contact (see, for instance, the slight delay of the peak and the waveform broadening of signal in B with respect to the signal in A). For its impact on the detector operation, the minimum distance to be implemented in order to overcome this border effect unavoidably becomes one of the most important layout rules for designing RSD.

Another crucial effect, related to the potential distribution along the *n*-type implant, is the so-called *voltage sag*. Being a resistive surface experiencing the current flow of multiplied electrons, the RSD cathode might be naturally subjected to a potential difference between the center and the outer part of the detector, where most of the current concentrates. From the same simulations just presented about the electric field trend, we observed that the voltage sag only slightly affects our RSD device. In panel (a) of Fig. 10 we reported the electrostatic potential as obtained from simulations at 160 V along an horizontal

cut located 10, 15 and 20 nm underneath the Silicon/oxide interface, i.e. through the resistive *n*-cathode. No voltage sag has to be noticed in these configurations (the slight decrease present within the first 50 μm is directly related to the field rise observed in Fig. 9). If the external bias increases (see panel (b) of Fig. 10) and, in general, when we are approaching the breakdown voltage (about 175 V in the simulation), the potential at a given depth progressively bends, producing a potential difference between AC-pad #1 and #3 of less than ~100 mV (for a leakage current of some μA). This means that, for the structure here considered and with the implants implemented, we are able to get rid of any sag effect when operating our RSD in a stable regime, i.e. suitably below the breakdown.

4.2. From spice-like to full-3D TCAD simulations of RSD

RSD simulations have been carried out in order to find the optimum range of the most important design parameters, such as the dielectric capacitance, the sheet resistance or the pad geometry. To this aim, Spice-like calculations accounting for the equivalent electrical model of Fig. 2(a) have been implemented. By injecting into the circuital nodes of the resistive sheet a test input signal – obtained through TCAD simulations of a 1D LGAD diode – one can read the output signal produced by the simplified model in any other point of the same grid.

Fig. 11 shows two relevant results coming from this procedure, which have been simulated by parametrizing some of the characteristic RSD figures of merit: the pad size in panel (a) and the sheet resistance in panel (b). In both graphs the same input signal has been injected (solid black) while, in the first case, the capacitance of each node has been changed to emulate a parallel plate capacitor with constant thickness (at its technological standard for the FBK foundry) and area as indicated by the legend. In the second case, the pad size has been kept fixed at 500×500 μm^2 and each resistor connecting two adjacent nodes has been modulated from 0.5 kΩ to 2 kΩ. As one may appreciate, as the pad size or the sheet resistance increases, the output response read on the same node (red dashed, dash-dotted and dotted curves) becomes higher in amplitude. We would like to stress that the test input signal we implemented have been created and injected just to probe the circuital properties of RSD as a preliminary test before knowing any device's feature. Only the output pulses are calculated by Spice simulation.

Having obtained an indication of what would be the region of interest for our basic design parameters, full-TCAD simulations have been performed. When not otherwise specified, the technological rules for dielectric thickness and ion implantation are set as their foundry standard to ensure an optimal AC-coupling. The first step consisted in implementing the 2D geometry reported in Fig. 9(a), with a 55 μm thickness and pitch of 50 μm, and simulating the AC-signals induced on all the three readout pads by a MIP heavy ion passing perpendicularly to the RSD and through the center of pad #1.

Fig. 12 reports the results of two different implant parametrizations. In panel (a) we tuned the *p*-gain dose by adding a 4% to the standard setup. As the acceptor concentration increases the signal amplitude becomes higher as well, without any significant modification of the peak time. A similar result is reported in panel (b) for the tuning of the *n*-cathode depth from the typical value to a deeper one. As one may notice, all the waveforms are bipolar. Indeed, as occurring in standard LGAD-based detectors and as predicted by the Ramo's theorem, the first lobe is due to the drift of multiplied electrons from the gain layer to the detector surface. Then, since the AC readout pads in RSD devices does not physically collect charges, when they move along the cathode towards the DC-contact, they produce an undershoot. Thus, the overall signal integral, given by both the induction and discharge contributions, is always null.

In order to directly see the effects of having different coupling capacitances, we simulated two RSD with the same features except for the dielectric thickness: Fig. 13(a) reports the simulated signals for a thin and a thick dielectric, showing that, as expected, the thinner the layer the strongest the AC-coupling, albeit the effect is rather mild.

The same figure, in panel (b), shows the comparison between the three usual signals simulated in 50 μm- and 100 μm-pitch devices. We notice that the signal induced in the readout pad where the particle hits the RSD sensor is larger when the pitch increases. In the case of the two nearest neighboring pads the signal waveforms tend to be longer but with a lower amplitude, determining also a forward shift of the peak. Such spreading in time of the signals on pads #2 and #3 is essentially due to the increase of their dimension, which determines a longer path for charge carriers before being completely seen by the readout.

After characterizing the electrical properties of RSD devices as a function of their technological parameters, it is useful to analyze the quality and the effectiveness of our simulations. In the framework of LGAD design, the implementation of a full geometry becomes critical only when we are interested in investigating the extremal behavior of those structures, as the breakdown phenomena. For such a purpose the inclusion of guard regions is almost mandatory. Similarly, in RSD, a realistic modeling could help in identifying some fundamental figures of merit such as, one among all, the capacitive coupling.

For these reasons now we want to answer the question: to what extend the 3D simulation of RSD is necessary? To this aim, a 1×3 structure as depicted on the right-hand side of Fig. 14(a) has been implemented. The rectangular metal region on top is, again, the DC-contact while colored square pads are the three AC-pads. On its left, the usual 2D version of the same RSD is reported for reference. In both structures the MIP heavy ion crosses the device perpendicularly to the central point of pad #1 (leftmost red pad).

As one may see in Fig. 14, the full-3D simulation gives a lower and broadened (in time) signal with respect to the 2D geometry, both in terms of AC- and DC-current. This can be probably due to the *space-charge effect*, not accounted for by the 2D simulation, caused by the high density of charges populating the resistive sheet during the signal freezing time. So, if by the standpoint of coupling properties the full-3D simulation results to be the only possible investigation, on the other hand, the parametric studies about all the RSD design and process rules are feasible just through the simple 2D geometry.

The last two topics that the authors want to report are a comparison between RSD and LGAD simulations, on one side, and the predicted performances of RSD in terms of radiation tolerance and acceptor deactivation, on the other one. The plots showing such results are reported in Fig. 15. Panel (a) includes a direct comparison between the electric profiles along the device vertical cut simulated in an LGAD and an RSD at the same bias voltage (150 V), and with the same *p*-gain implants. What we can infer is that, for a given gain layer concentration and due to the different *n*-cathode implant with respect to the traditional technology, the multiplication occurs closer to the silicon surface in the RSD than in the LGAD. Moreover, the field intensity is higher for the first device, probably leading to more critical breakdown voltages with respect to the traditional silicon technology for 4D particle tracking.

To explore the radiation tolerance of RSD and the degradation of signals with fluence, in case of their use for 4D-tracking in radiation-intense environments, 2D numerical simulations have been carried out. By implementing both the creation of acceptor-like traps in the bulk (which acts on the detector resistivity) and the Boron deactivation in the gain layer – as modeled by Eq. (11) – the results shown in Fig. 15(b) have been obtained. As usual, simulated signals are triggered by a MIP heavy ion crossing the device in the center of the AC-pad #1, the same in which the charge is read. In the case of AC-coupled signals, only the positive lobe of the current waveform has been accounted for in calculating the induced charge, while for the DC-contact the entire signal shape has been integrated in time. Notice that the radiation resistance at high fluence corresponding to the capacitive coupling is sightly better than the trend obtained for the traditional DC readout, where less than the 20% of the original signal survives beyond 10^{15} n_{eq}/cm^2. Such behavior is quite well matching the experimental data coming from a UFSD2 sample with the same *p*-gain implant. This result could be interpreted as the effect of having a higher electric field in the RSD compared to the corresponding LGAD, as shown in the same figure.

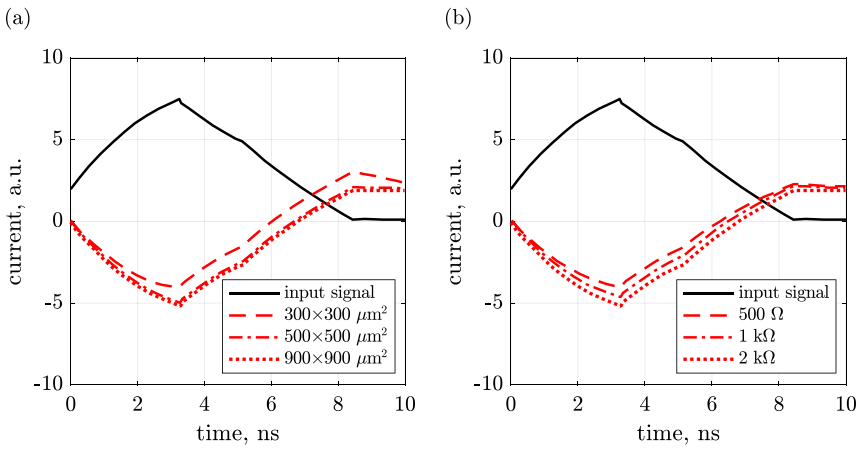

Fig. 11. RSD response (red curves) of a TCAD-like input signal (solid black) simulated with Spice as a function of (a) the AC-pad size and (b) sheet resistance. The signal is injected and read on the same node of the resistive grid, as represented in the electrical model of Fig. 2(a).

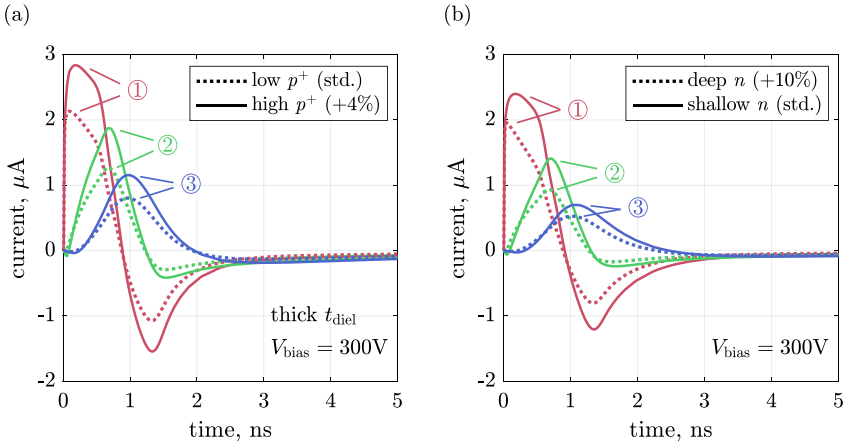

Fig. 12. TCAD simulations of AC-coupled signals generated in a 50 μm-pitch three-pad RSD sensor (the circled numbers identify the position of the pad, from left to right) by a MIP heavy ion for (a) two *p*-gain doses and (b) *n*-cathode depths. The parametric setup is the standard one in the right plot while in the first one a thick dielectric has been implemented.

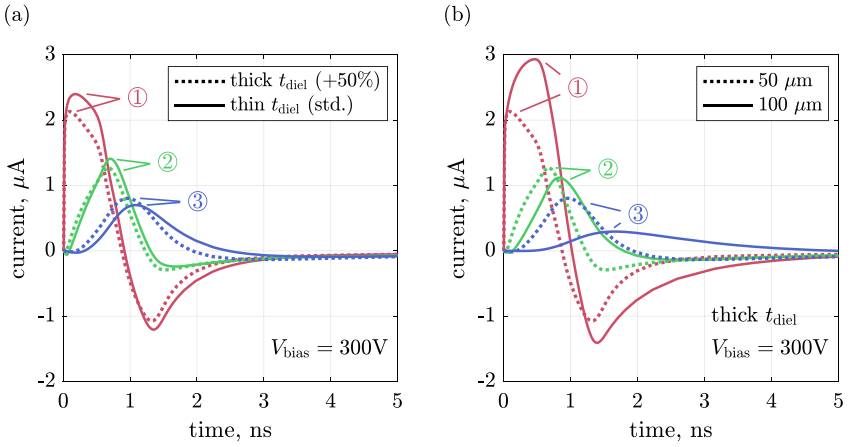

Fig. 13. TCAD simulations of AC-coupled signals generated in a 50 μm-pitch three-pad RSD sensor (the circled numbers identify the position of the pad, from left to right) by a MIP heavy ion for (a) two dielectric thicknesses and (b) pad pitches. The parametric setup is the standard one in the left plot while in the second one a thick dielectric has been implemented.

5. Comments and conclusions

In this paper, advanced and reliable techniques to model and characterize silicon particle detectors for 4D-tracking through device-level numerical simulation have been reviewed. As a case-study we analyzed the LGAD technology and, in particular, the RSD sensors. After a summary of the main devices figures of merit, we moved to the framework of Technology Computer-Aided Design (TCAD) physics-based numerical simulation, giving some relevant examples of its powerful capabilities in predicting the electrical behavior of real devices. To this

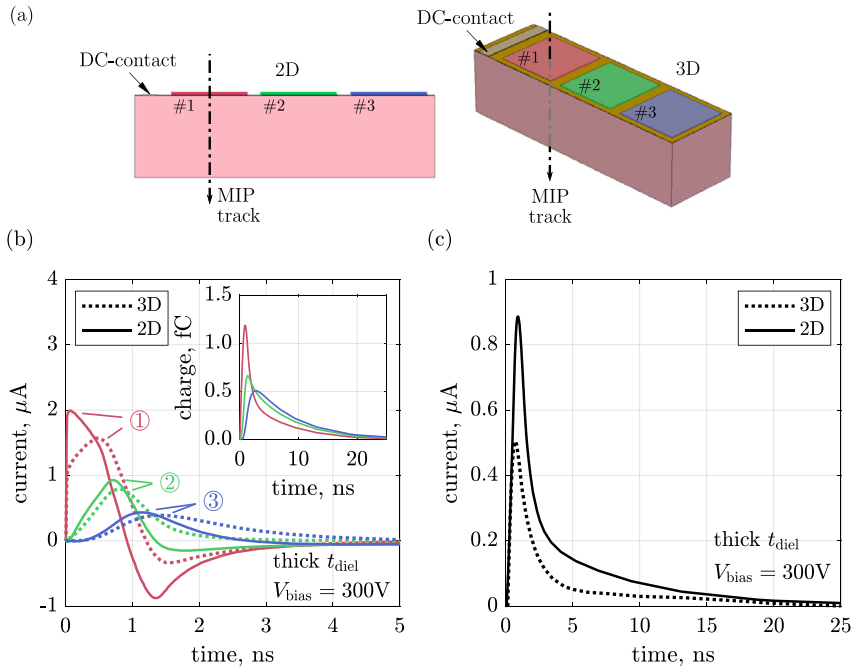

Fig. 14. Panel (a): 2D and 3D geometry of the simulated RSD where also the MIP heavy ion track, passing through pad #1, is represented in both cases. Panel (b): simulated AC-signals induced on the three readout pads (inset: integrated charge versus time for the 2D simulations). Panel (c): simulated current density versus time collected by the DC-contact. Note: simulations refer to a 60 μm-pitch RSD device. (For interpretation of the references to color in this figure legend, the reader is referred to the web version of this article.)

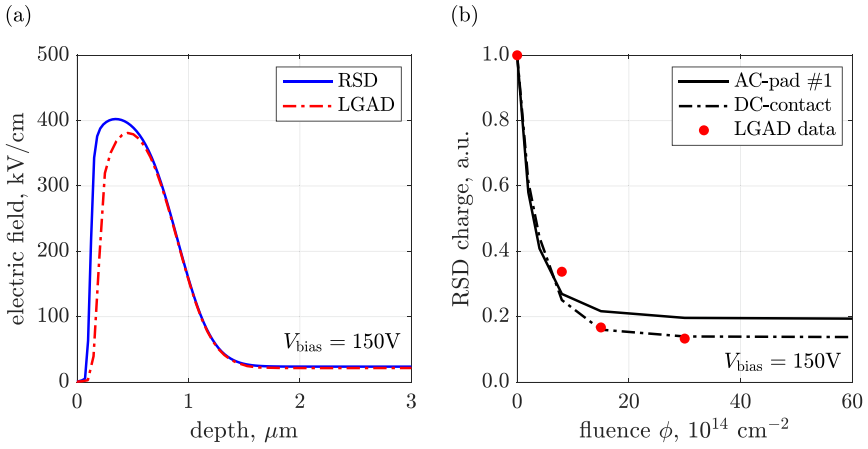

Fig. 15. Panel (a): electric field profile along a vertical cut of (unirradiated) RSD and LGAD devices having the same *p*-gain implant, simulated at 150 V. Panel (b): simulated (normalized) charge degrading with fluence in an RSD device for both AC and DC signals (lines), along with a data set (dots) taken at the same bias voltage on an LGAD device from the UFSD2 run.

aim a calibration procedure has been presented: through simple-2D simulation of *p-i-n* diodes and the comparison with the corresponding experimental data, it is possible to extract several technology- and device-related parameters to be used for optimizing the implemented physical models. After such calibration procedure, the simulations of LGAD have been extensively described in terms of electrostatic behavior and radiation-tolerance performances. Finally, the RSD paradigm has been introduced and then analyzed by means of both Spice-like and 2D/3D TCAD simulations, always with the main focus of designing and optimizing new structures for particle tracking.

The methodological approach here described demonstrated to be robust and reliable, having allowed so far to successfully release three productions of UFSD and one of RSD. Moreover, numerical simulations are the only available tool to predict the detectors performance and to extract the set of technological parameters needed to implement proper layout rules for their design, on the first hand, and correct process flows at the fabrication stage, on the second one. Finally, device-level numerical calculations – although they require delicate calibrations – are fundamental also in determining the detectors lifetime and their aging in terms of radiation-induced damage and performance degradation.

From the results here presented we can conclude that our numerical framework is well calibrated with respect to the simulation of current and charges as a function of the applied bias, as well as with the increasing fluence. Furthermore, we found that full-3D simulations can be avoided for generic design purposes, as the parametric study of several geometric and technological variables or the investigation about their relative weights, but is mandatory to properly predict the absolute amount of induced charges and, thus, in calculating the AC-coupled signals. This is probably due to the fact that only 3D calculations are embedding important electrostatic properties, such the space-charge effect induced by the high carriers concentration.

Exploiting the predictive power of numerical calculations we designed at INFN Torino the run of sensors named RSD1, released by

FBK in June 2019 and currently under testing. This production will be the definite workbench of our methodological approach and, in the meanwhile, will also represent the basis for both a characterization of a novel kind of 4D particle trackers and their optimization in view of a following production run.

Declaration of competing interest

The authors declare that they have no known competing financial interests or personal relationships that could have appeared to influence the work reported in this paper.

CRediT authorship contribution statement

M. Mandurrino: Conceptualization, Methodology, Software, Validation, Formal analysis, Investigation, Resources, Data curation, Writing - original draft, Writing - review & editing, Visualization, Project administration, Funding acquisition. **R. Arcidiacono:** Validation, Resources. **M. Boscardin:** Resources. **N. Cartiglia:** Conceptualization, Methodology, Validation, Investigation, Resources, Writing - review & editing, Funding acquisition. **G.-F. Dalla Betta:** Investigation, Writing - review & editing. **M. Ferrero:** Investigation, Data curation. **F. Ficorella:** Investigation, Data curation. **L. Pancheri:** Investigation, Writing - review & editing. **G. Paternoster:** Investigation, Data curation. **F. Siviero:** Investigation, Data curation. **V. Sola:** Investigation, Data curation. **A. Staiano:** Investigation. **A. Vignati:** Investigation.

Acknowledgments

This work and the RSD project are supported by INFN, Italy Gruppo-V through the "2017 Young Researchers Grant" funding program (as in the INFN announcement No. 19105 and the related deliberation No. 19567). The authors would also thank the RD50 Collaboration at CERN and UC Santa Cruz for the scientific endorsement.

Appendix. Parameters for the modeling of charge multiplication

Now we describe how the electron/hole impact ionization coefficients $\alpha_{n,p}$ are parametrized for all the three models here employed in the numerical implementation of avalanche processes. By definition, $\alpha_{n,p}$ (in cm^{-1}) corresponds to the inverse of the electron/hole mean free path between two subsequent scattering events, which give rise to the impact ionization of lattice atoms. When the field driving charge carriers becomes such that this process cannot be naturally damped anymore, and carriers overcome a certain critical velocity, then the avalanche multiplication starts. The coefficients $\alpha_{n,p}$ describe in a macroscopic scale such mechanism, being the representation of how the mean free path decreases as a function of the increasing electric field.

As we have seen in the previous sections, the ionization coefficients follow the so-called Chynoweth law [13], where the exponential growth is multiplied by a certain pre-factor. According to the physical model, each term has a particular parametrization, coming from different experimental data taken on different samples of silicon devices. In particular, for the Massey formula [10] we have that

$$\begin{aligned} A_n^{\mathrm{Mas}} &= 4.43 \cdot 10^5\ \mathrm{cm}^{-1} \\ A_p^{\mathrm{Mas}} &= 1.13 \cdot 10^6\ \mathrm{cm}^{-1} \end{aligned} \tag{14}$$

and

$$\begin{aligned} B_n^{\mathrm{Mas}}(T) &= C_n^{\mathrm{Mas}} + D_n^{\mathrm{Mas}} \cdot T \\ B_p^{\mathrm{Mas}}(T) &= C_p^{\mathrm{Mas}} + D_p^{\mathrm{Mas}} \cdot T \end{aligned} \tag{15}$$

where

$$\begin{aligned} C_n^{\mathrm{Mas}} &= 9.66 \cdot 10^5\ \mathrm{V/cm} \\ C_p^{\mathrm{Mas}} &= 1.71 \cdot 10^6\ \mathrm{V/cm} \end{aligned} \tag{16}$$

and

$$\begin{aligned} D_n^{\mathrm{Mas}} &= 4.99 \cdot 10^2\ \mathrm{V\ cm^{-1}\ K^{-1}} \\ D_p^{\mathrm{Mas}} &= 1.09 \cdot 10^3\ \mathrm{V\ cm^{-1}\ K^{-1}} \end{aligned} . \tag{17}$$

In the same way, we have the parameters for van Overstraeten–de Man [11]

$$\begin{aligned} A_n^{\mathrm{vOv}} &= 7.030 \cdot 10^5\ \mathrm{cm}^{-1} \\ B_n^{\mathrm{vOv}} &= 1.231 \cdot 10^6\ \mathrm{V/cm} \end{aligned} , \tag{18}$$

$$\begin{aligned} A_p^{\mathrm{vOv}} &= 1.582 \cdot 10^6\ \mathrm{cm}^{-1} \quad (\text{below } 4 \cdot 10^5\ \mathrm{V/cm}) \\ B_p^{\mathrm{vOv}} &= 2.036 \cdot 10^6\ \mathrm{V/cm} \quad (\text{below } 4 \cdot 10^5\ \mathrm{V/cm}) \\ A_p^{\mathrm{vOv}} &= 6.710 \cdot 10^5\ \mathrm{cm}^{-1} \quad (\text{above } 4 \cdot 10^5\ \mathrm{V/cm}) \\ B_p^{\mathrm{vOv}} &= 1.693 \cdot 10^6\ \mathrm{V/cm} \quad (\text{above } 4 \cdot 10^5\ \mathrm{V/cm}) \end{aligned} \tag{19}$$

and

$$\gamma = \frac{\tanh\left(\frac{\hbar\omega_{\mathrm{op}}}{2k_{\mathrm{B}}300\mathrm{K}}\right)}{\tanh\left(\frac{\hbar\omega_{\mathrm{op}}}{2k_{\mathrm{B}}T}\right)}, \tag{20}$$

where $\hbar\omega_{\mathrm{op}} = 0.063\,\mathrm{eV}$ is the optical phonon energy in silicon, and for the Okuto–Crowell model [12]

$$\begin{aligned} A_n^{\mathrm{Oku}} &= 0.426\,\mathrm{V}^{-1} \\ A_p^{\mathrm{Oku}} &= 0.243\,\mathrm{V}^{-1} \\ B_n^{\mathrm{Oku}} &= 4.81 \cdot 10^5\ \mathrm{V/cm} \\ B_p^{\mathrm{Oku}} &= 6.53 \cdot 10^5\ \mathrm{V/cm} \end{aligned} \tag{21}$$

and

$$\begin{aligned} C_n^{\mathrm{Oku}} &= 3.05 \cdot 10^{-4}\,\mathrm{K}^{-1} \\ C_p^{\mathrm{Oku}} &= 5.35 \cdot 10^{-4}\,\mathrm{K}^{-1} \\ D_n^{\mathrm{Oku}} &= 6.86 \cdot 10^{-4}\,\mathrm{K}^{-1} \\ D_p^{\mathrm{Oku}} &= 5.67 \cdot 10^{-4}\,\mathrm{K}^{-1} \end{aligned} . \tag{22}$$

References

[1] N. Cartiglia, et al., Design optimization of UFSD silicon detectors, Nucl. Instrum. Methods Phys. Res. A 796 (2015) 141–148, http://dx.doi.org/10.1016/j.nima.2015.04.025.

[2] H.F.-W. Sadrozinski, A. Seiden, N. Cartiglia, 4D tracking with ultra-fast silicon detectors, Rep. Progr. Phys. 81 (2018) 026101, http://dx.doi.org/10.1088/1361-6633/aa94d3.

[3] N. Cartiglia, et al., Beam test results of a 16ps timing system based on ultra-fast silicon detectors, Nucl. Instrum. Methods Phys. Res. A 850 (2017) 83–88, http://dx.doi.org/10.1016/j.nima.2017.01.021.

[4] CMS Collaboration, Technical proposal for a MIP timing detector in the CMS experiment Phase 2 upgrade, CERN-LHCC-2017-027; LHCC-P-009.

[5] J. Bendavid, MIP timing detector for CMS phase-II upgrade, in: CMS MTD Meeting, CERN, 2018.

[6] M. Mandurrino, et al., First demonstration of 200, 100, and 50 μm pitch resistive AC-coupled silicon detectors (RSD) with 100% fill-factor for 4D particle tracking, 2019, arXiv:1907.03314.

[7] M. Mandurrino, et al., TCAD simulation of silicon detectors: A validation tool for the development of LGAD, in: 30th RD50 Workshop, Kraków, 2017.

[8] M. Mandurrino, et al., Numerical simulation of charge multiplication in ultra-fast silicon detectors and comparison with experimental data, in: 2017 IEEE Nuclear Science Symposium and Medical Imaging Conference, NSS/MIC, Atlanta, 2017, http://dx.doi.org/10.1109/NSSMIC.2017.8532702.

[9] Sentaurus Device User Guide, Version N-2017.09, Synopsys, Inc., Mountain View, CA, 2017.

[10] D.J. Massey, J.P.R. David, G.J. Rees, Temperature dependence of impact ionization in submicrometer silicon devices, IEEE Trans. Electron Devices 53 (9) (2006) 2328–2334, http://dx.doi.org/10.1109/TED.2006.881010.

[11] R. van Overstraeten, H. de Man, Measurement of the ionization rates in diffused silicon p–n junctions, Solid-State Electron. 13 (5) (1970) 583–608, http://dx.doi.org/10.1016/0038-1101(70)90139-5.

[12] Y. Okuto, C.R. Crowell, Threshold energy effect on Avalanche breakdown voltage in semiconductor junctions, Solid-State Electron. 18 (2) (1975) 161–168, http://dx.doi.org/10.1016/0038-1101(75)90099-4.

[13] A.G. Chynoweth, Ionization rates for electrons and holes in silicon, Phys. Rev. 109 (5) (1958) 1537–1540, http://dx.doi.org/10.1103/PhysRev.109.1537.

[14] B.R. Gossick, Disordered regions in semiconductors bombarded by fast neutrons, J. Appl. Phys. 30 (8) (1959) 1214–1218, http://dx.doi.org/10.1063/1.1735295.
[15] G. Kramberger, et al., Radiation effects in low gain Avalanche detectors after hadron irradiations, J. Inst. 10 (7) (2015) P07006, http://dx.doi.org/10.1088/1748-0221/10/07/P07006.
[16] G.D. Watkins, EPR studies of lattice defects in semiconductors, in: B. Henderson, A.E. Hughes (Eds.), Defects and their structure in non-metallic solids, Plenum, New York, 1976, http://dx.doi.org/10.1007/978-1-4684-2802-5_7.
[17] R. Wunstorf, W.M. Bugg, J. Walter, F.W. Garber, D. Larson, Investigations of donor and acceptor removal and long term annealing in silicon with different boron/phosphorus ratios, Nucl. Instrum. Methods A 377 (1–2) (1996) 228–233, http://dx.doi.org/10.1016/0168-9002(96)00217-3.
[18] J.P. Balbuena, et al., RD50 Status Report 2008 - Radiation hard semiconductor devices for very high luminosity colliders, CERN-LHCC-2010-012; LHCC-SR-003, CERN, Geneva, 2008, URL: http://cds.cern.ch/record/1291631.
[19] M. Ferrero, et al., Radiation resistant LGAD design, Nucl. Instrum. Methods A 919 (2019) 16–26, http://dx.doi.org/10.1016/j.nima.2018.11.121.
[20] W. Shockley, Currents to conductors induced by a moving point charge, J. Appl. Phys. 9 (10) (1938) 635–636, http://dx.doi.org/10.1063/1.1710367.
[21] S. Ramo, Currents induced by electron motion, Proc. IRE 27 (9) (1939) 584–585, http://dx.doi.org/10.1109/JRPROC.1939.228757.
[22] G. Kramberger, et al., Radiation hardness of thin low gain Avalanche detectors, Nucl. Instrum. Methods Phys. Res. A 891 (2018) 68–77, http://dx.doi.org/10.1016/j.nima.2018.02.018.
[23] G. Kramberger, Results and plans on irradiated LGAD sensors, in: High Granularity Timing Detector (HGTD) Meeting, CERN, 2017.
[24] V. Eremin, et al., Development of transient current and charge techniques for the measurement of effective net concentration of ionized charges (N_{eff}) in the space charge region of p–n junction detectors, Nucl. Instrum. Methods Phys. Res. A 372 (3) (1993) 388–398, http://dx.doi.org/10.1016/0168-9002(95)01295-8.
[25] H.F.-W. Sadrozinski, Timing measurements on ultra-fast silicon detectors, in: 12th Trento Workshop on Advanced Silicon Radiation Detectors, Trento, 2017.
[26] G. Kramberger, Radiation hardness of thin LGAD detectors, in: 12th Trento Workshop on Advanced Silicon Radiation Detectors, Trento, 2017.
[27] V. Sola, et al., First FBK production of 50μm ultra-fast silicon detectors, Nucl. Instrum. Methods Phys. Res. A 924 (2019) 360–368, http://dx.doi.org/10.1016/j.nima.2018.07.060.